The Astronomical Radio Transient Experiment (ARTE): assembly, integration, and verification

F.Solís[a], R.Finger[b,c], D.Gallardo[c], S.Jorquera[d], D.Monasterio[c], W.Max-Moerbeck[b], M.Prieto[b], T.Cassanelli[c], M.Cruces[e], C.San Martín[b], J.Retamal[b], J.Pizarro [b], C.Avilés[f], C. Espinoza[g], and L.Bronfmann[b]

[a]Atacama Large Millimeter Array, ALMA, Santiago, Chile
[b]Department of Astronomy, Universidad de Chile, Santiago, Chile
[c]Department of Electrical Engineering, Universidad de Chile, Santiago, Chile
[d]Atacama Pathfinder Experiment, APEX, Atacama, Chile
[e]Department of Astronomy, Universidad Católica, Santiago, Chile
[f]European Southern Observatory, Garching, Germany
[g]National Radio Astronomy Observatory, Charlottesville, Virginia, USA

ABSTRACT

The Astronomical Radio Transient Experiment (ARTE) is a novel proof-of-concept radio telescope designed, assembled, and integrated at the Millimeter Wave Laboratory (MWL) at the National Astronomical Observatory of the University of Chile[1] for the real-time detection of bright Galactic Fast Radio Bursts (FRB)-like events. Motivated by the absence of dedicated FRB instrumentation in Chile, ARTE is engineered to continuously track the Galactic Center using an elongated beam pattern[2] designed to match the Galactic disk, maximizing the probability of detecting bright radio transients originating within the Milky Way. The system is inspired by the Survey for Transient Astronomical Radio Emission 2 (STARE2),[3] which incorporates a single-site antenna array, with 600 MHz instantaneous bandwidth. Real-time post-channelization correction of the dispersive delay (also known as incoherent dedispersion[4]) is implemented on a Virtex-6 SX475T Field Programmable Gate Array[5] (FPGA). The instrument achieves a minimum detectable fluence of 131.45 kJy for millisecond-duration events at 1.5 GHz, targeting bright Galactic FRB-like bursts.

This work presents the assembly, integration, and verification of the ARTE instrument, including the Radio Frequency (RF) frontend, digital signal processing chain, and real-time transient detection pipeline. Commissioning observation validated the end-to-end operation of the system through the detection of astrophysical signals, artificial radio sources, and injected FRB-like signals, demonstrating the potential of a low-cost, wideband radio telescope dedicated to transient events.

Keywords: Fast Radio Bursts (FRBs), antenna array, dual polarization, Field Programmable Gate Array (FPGA), incoherent dedispersion, Direction of Arrival (DoA), Radio Frequency Interference (RFI), Radio telescope

1. INTRODUCTION

Fast Radio Bursts (FRBs) are brief astrophysical transients characterized by microsecond-to-millisecond durations, flux densities ranging from a few to hundreds of Jansky (Jy), and extremely high brightness temperatures ($T_B \gtrsim 10^{36}$ K).[6] These bursts appear as short-lived pulses that span a broad spectral range from roughly 100 MHz to about 8 GHz. As FRB signals propagate through the interstellar medium (ISM) and the intergalactic medium (IGM), interactions with free electrons along the line-of-sight introduce a frequency-dependent delay known as Dispersion Measure[7] (DM). Detecting these dispersed signals in real-time becomes complex because

Further author information: (Send correspondence to Francisca Solís.)
Francisca Solís: E-mail: francisca.solis@alma.cl, Telephone: +56957844886

Radio Telescopes, Technologies, and Methods, edited by Joseph Lazio, Ming-Tang Chen, Stefan J. Wijnholds
Proc. of SPIE Vol. 14153, 141531K · 2026 Published by SPIE
0277-786X · doi: 10.1117/12.3102859

FRBs are often barely above the noise floor, making them difficult to distinguish with most of the telescopes that integrate signals over long observing times.
Although their physical origin remains uncertain, current evidence strongly suggests a connection with highly magnetized neutron stars, particularly after the detection of radio bursts from the Galactic magnetar SGR 1935 + 2154.[8] Continuous monitoring of the radio sky is key to improving the understanding of magnetars, the structure of the Milky Way, the magnetic properties of the ISM, and the transient radio sky, and at the same time contributes to the broader understanding of high-energy astrophysical phenomena.
Motivated by the absence of dedicated FRB instrumentation in Chile, the Astronomical Radio Transient Experiment was developed as a low-cost proof-of-concept radio telescope for the real-time detection of bright Galactic FRB-like events. Inspired by the STARE-2 experiment, ARTE combines a compact antenna array, wide instantaneous bandwidth, and real-time digital signal processing to continuously monitor the Galactic center region.

This paper presents the design, assembly, integration, and verification of the ARTE instrument, including the antenna array, radio receiver chain, digital backend, and transient detection pipeline.

2. SYSTEM OVERVIEW

2.1 Simplified instrument architecture

The ARTE instrument is installed inside a protective dome incorporating a Radio Frequency (RF) transparent window to enable continuous observations while minimizing environmental exposure. Figure 1 presents a simplified overview of instrument architecture and signal flow. The system consists of the main antenna array, a reference antenna for RFI monitoring, a direct radio receiver chain per sub-array, and a digital backend implemented on a ROACH2[9] platform. The following sections describe each subsystem in general technical detail.

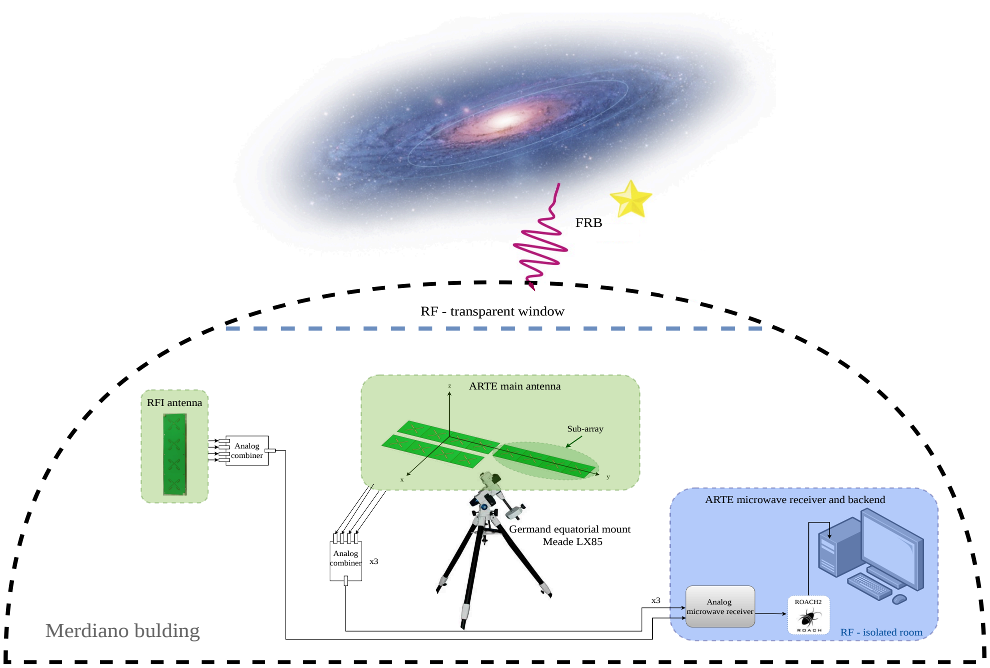

Figure 1: Simplified block diagram of the ARTE instrument architecture. The main antenna array continuously tracks the Galactic Center, while a secondary fixed-position antenna monitors the local RFI environment. Signals are amplified, filtered, digitized, and processed in real time by the ROACH2 backend for channelization, incoherent dedispersion, transient detection, and RFI mitigation. Low-time-resolution spectra are continuously stored for offline analysis, while high-time-resolution raw data are dumped to disk whenever a trigger is generated.

2.2 Specifications

ARTE was conceived as a cost-effective and simplified version of STARE-2, with system specifications defined to optimize sensitivity, sky coverage, source localization, and RFI mitigation. Since pulsars and FRB-like events are expected to be predominantly concentrated toward the Galactic plane, the antenna array was designed to produce an elliptical beam pattern covering the Galactic Center region. To satisfy this requirement while maintaining a compact architecture, a single-site array of dual-polarization dipoles was adopted. The operational frequency range between 1.2 GHz and 1.8 GHz was selected to reduce the antenna size and overall cost of the system while maintaining adequate sensitivity for FRB observations. In addition, the instrument was designed to provide source localization capabilities through the DoA algorithm, as well as RFI mitigation using an auxiliary omnidirectional antenna and channel-flagging techniques. Finally, the digital backend was designed to support real-time incoherent dedispersion, transient triggering, and raw-data dumps with high temporal resolution.

Table 1: ARTE technical specifications

Parameter	Measured at 1.5 GHz
Frequency range (Δf)	1.2 - 1.8 GHz
Bandwidth (BW)	600 MHz
Gain (G)	65.50 dB
Noise temperature (T_{sys})	161 K
Fluence ($\mathcal{F}$)	131.45 kJy ms
Polarization	linear dual-pol

2.3 Observing strategy

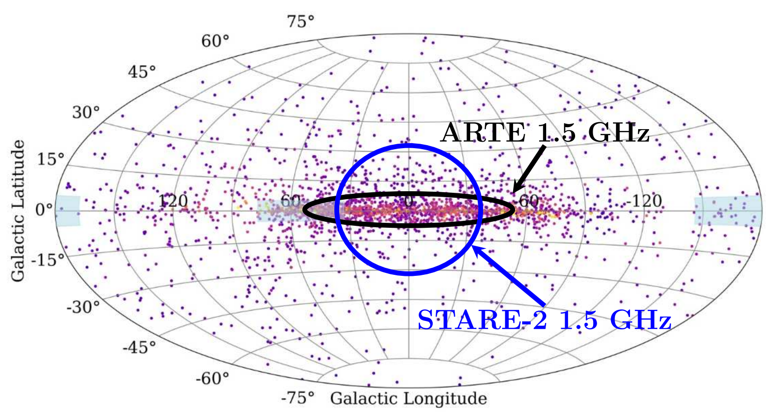

Figure 2: This figure compares the projected radiation patterns of the STARE-2 and ARTE antenna arrays at 1.5 GHz over the Galactic plane in Galactic coordinates (l, b), together with the distribution of known pulsars, which are predominantly concentrated toward the central region of the Milky Way. The ellipses represent the corresponding half-power beamwidths (HPBWs) of each instrument.Reproduced from[2]

To maximize the probability of detecting a Galactic burst, it is assumed that the pulsar distribution follows the scheme shown in Figure 2, which is broadly concentrated within the Milky Way. Given the similar astrophysical nature of pulsars and FRBs, a comparable spatial distribution is expected.

Based on this assumption, the observing strategy consists of continuous tracking of the Milky Way whenever the Galactic center is located at elevations higher than 30° above the horizon. When this condition is not satisfied, and the source is no longer observable, the beam is directed toward the intersection between the Galactic plane and the (30° elevation line above the horizon); if this configuration is not possible, the beam is pointed toward the zenith.

To facilitate continuous tracking and compensate for Earth's rotation, an equatorial mount is used. In particular, the German equatorial mount LX85 was selected due to its suitability for implementing a customized tracking strategy.

As previously mentioned, this project is inspired by the STARE-2 experiment. One of the main improvements with respect to STARE-2 is the beam pattern design, which is optimized so that its sky projection matches the Milky Way. With this in mind, the beam specifications are defined as $\mathrm{HPBW_x} > 80°$ and the $\mathrm{HPBW_y} < 15°$, resulting in an elliptical beam pattern that maximizes coverage of the Galactic plane.

3. ANTENNA ARRAY, RECEIVER SYSTEM AND DIGITAL BACKEND

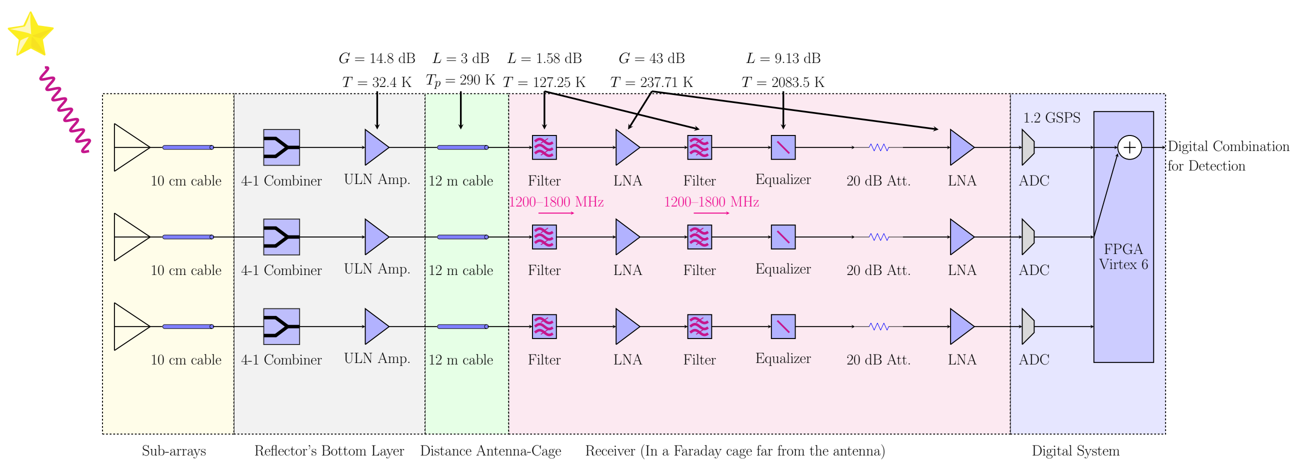

Figure 3: Instrument architecture from the antenna array to the digital system

3.1 Antenna array

In this work, only the main architectural aspects of the antenna array are presented. The detailed description of the antenna design, including electromagnetic simulations, mechanical implementation, optimization procedures, and subsystem validation, is provided by Gallardo et al.[2] Since the primary focus of this paper is the Assembly, Integration and Verification (AIV) process and commissioning of the complete instrument, those aspects are not discussed further.

The antenna subsystem consists of three sub-arrays arranged in an L shape, as shown in Figure 4. Each sub-array comprises four dual-polarization dipole elements operating in the 1.2 - 1.8 GHz frequency range. The two sub-arrays aligned along the y-axis are sufficient to generate the elongated beam pattern required to maximize sensitivity toward the Galactic plane. The third sub-array was incorporated to enable DoA estimation, resulting in the final L-shaped geometry. In addition, an aluminum reflector plane was installed at a distance of approximately $\frac{\lambda}{4}$ behind the antenna elements, increasing the front-to-back ratio beyond the required 10 dB

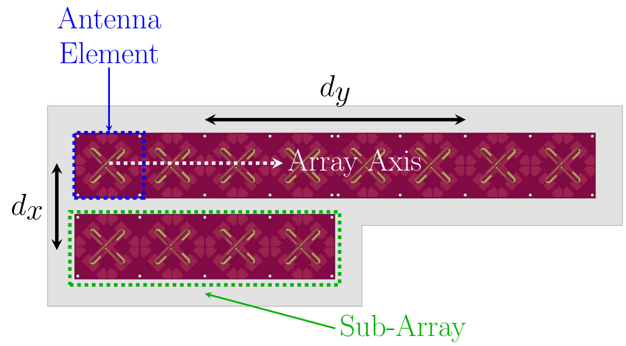

Figure 4: High Frequency Structure Simulator (HFSS) model of the main antenna array

specification.

Each antenna element provides two orthogonal linear polarization outputs. This capability was incorporated because FRBs can exhibit a wide range of polarization characteristics, as documented by Petroff,[10] while the polarization state and orientation of a potential transient source cannot be predicted before detection. Dual polarization reception, therefore, ensures sensitivity to signals regardless of their incoming polarization orientation. Although the instrument supports dual-polarization operation, the AIV campaign and commissioning observations reported in this work were conducted using a single polarization channel. Further observing campaigns will incorporate both polarizations.

3.1.1 Beam pattern

Figure 5 presents the simulated and measured radiation patterns in the orthogonal x- and y-planes at the center frequency of 1.5 GHz, as well as at lower and upper limits of the ARTE operating bandwidth (1.2 GHz and 1.8 GHz, respectively). The measurements were obtained by coherently combining the eight antenna elements along the y-axis, corresponding to the configuration that allows the detection.

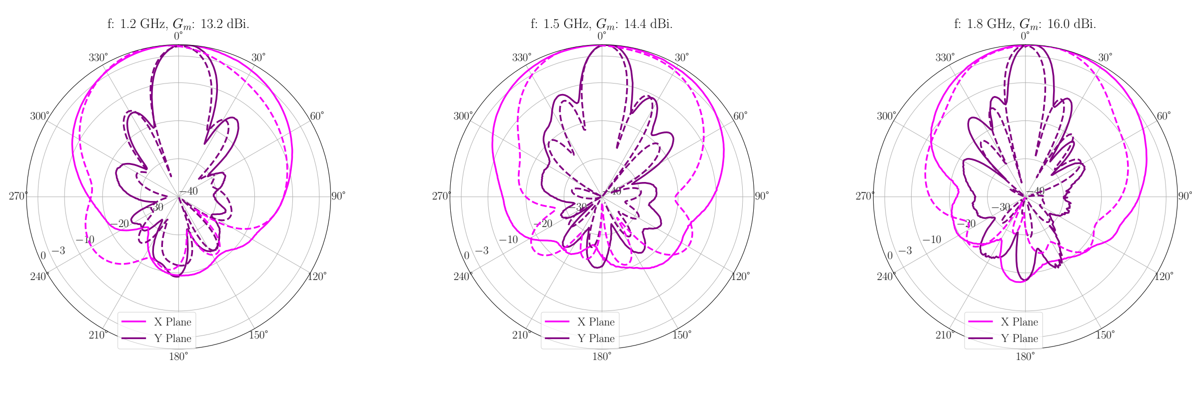

(a) (b) (c)

Figure 5: Measured (solid lines) and simulated (dashed lines) radiation patterns of the L-shaped antenna array considering the feeding of 8 consecutive elements. Measurements are normalized with respect to their maximum, and simulations are normalized with respect to their maximum (G_m).

The radiation patterns are normalized to their respective peak gains, while the values for HPBWs and FBRs are summarized in the following Table 2. Good agreement is observed between simulations and measurements.

The main lobes exhibit similar amplitudes and pointing directions across the entire frequency range. Although some measured sidelobes are higher than those predicted by the simulations, their levels remain below 10 dB relative to the main lobe.
Furthermore, the measured FBR remains close to 20 dB throughout the operating bandwidth. According to the criterion established in the specification, an FBR exceeding 10 dB ensures that the signals arriving through the back lobe are negligible.[2]

Table 2: Simulated and measured radiation characteristics of the antenna.

	1200 MHz		**1500 MHz**		**1800 MHz**	
Parameter	Sim.	Meas.	Sim.	Meas.	Sim.	Meas.
HPBW_x	54°	80°	70°	97.5°	55°	80°
HPBW_y	17°	20°	13°	15°	12.5°	15°
Front-to-Back Ratio	22 dB	19 dB	26 dB	21 dB	29 dB	18 dB

3.2 Direct radio receiver chain

The radio receiver was developed for the ARTE telescope as part of an undergraduate thesis project.[11] Following its initial implementation, several modifications were introduced during the commissioning phase to improve system performance and address issues identified during the integration. These modifications are discussed in Subsection 4. The final receiver architecture is shown in Figure 6, while the Table 3 summarizes the commercial components used in this implementation.

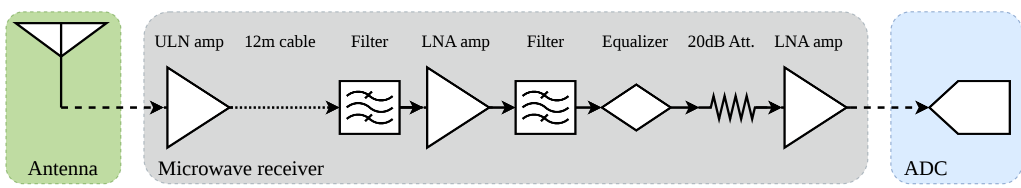

Figure 6

Table 3: Radio receiver chain components and main specifications

Stage	**Component**	**Model**	**Main specifications @ 1.5 GHz**
ULN	Commercial amp.	ZX60-P33ULN[12]	Gain 14.8 dB NF 0.46 dB
Band-pass filter	Custom desing	not applicable	BW ≈ 540MHz
LNA	Commercial amp.	ZX60-2534MA[13]	Gain 43.42 dB NF 2.24 dB
Equalizer	Commercial amp.	ZEQ-8-222S+[14]	insertion loss ≈ 9.13, dB
Attenuator	Commercial att.	VAT-20+[15]	att. ≈ 20.25 dB
RF interconnection	Coaxial SMA cable	LM200	12 m insertion loss ≈ 3 dB

From Figure 6, a direct radio receiver architecture operating in the third Nyquist zone was implemented to satisfy the requirements. Finally, in Figure 7a, two RF chains are compared (the chains used to combine the main beam pattern). The operation frequency is from 1.24 GHz to 1.74 GHz, with a total measured gain of 65.5 dB, which is consistent with the theoretical calculation shown in Equation 4. The only non-commercial component of the receiver chain is the custom band-pass filter, and Figure 7b presents the measured reflection and transmission coefficients response from the interest bandwidth.

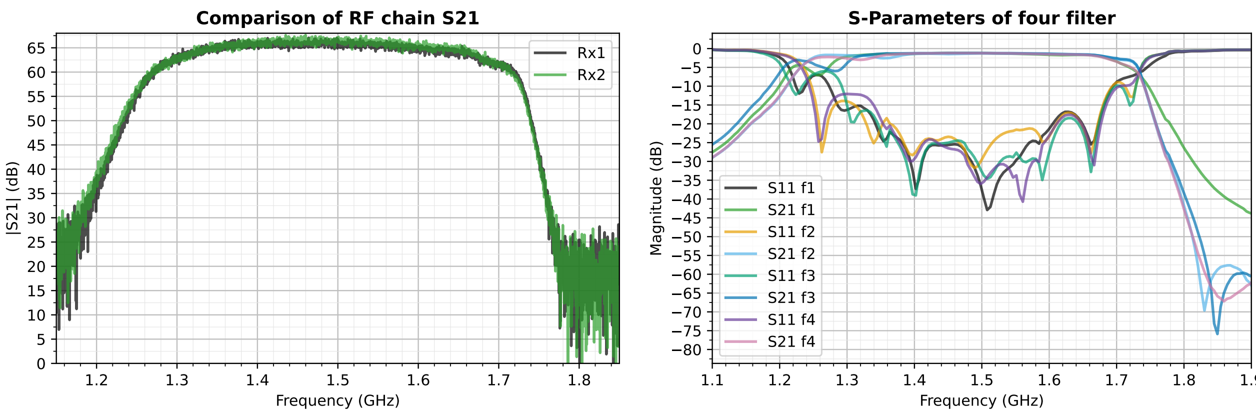

(a) S21 comparison between the receivers of the main beam

(b) S11 and S21 between filters

Figure 7: Left : Measured frequency responses of S21 (transmission coefficient) of main RF chains. Right: Measured frequency responses of S11 (input reflection coefficient) and S21 between four filters.

Based on the Friis equation,[16] the theoretical noise temperature of the receiver chain is given by the following expression,

$$\begin{aligned}\mathrm{T_{rx}} = \mathrm{T_{ULN}} &+ \frac{\mathrm{T_{cable}}}{\mathrm{G_{ULN}}} \\ &+ \frac{\mathrm{T_{F_1}}}{\mathrm{G_{ULN}L_{cable}^{-1}}} \\ &+ \frac{\mathrm{T_{LNA}}}{\mathrm{G_{ULN}L_{cable}^{-1}L_{F_1}^{-1}}} \\ &+ \frac{\mathrm{T_{F_2}}}{\mathrm{G_{ULN}L_{cable}^{-1}L_{F_1}^{-1}G_{LNA}}} \\ &+ \frac{\mathrm{T_{EQ}}}{\mathrm{G_{ULN}L_{cable}^{-1}L_{F_1}^{-1}G_{LNA}L_{F_2}^{-1}}} \\ &+ \frac{\mathrm{T_{att}}}{\mathrm{G_{ULN}L_{cable}^{-1}L_{F_1}^{-1}G_{LNA}L_{F_2}^{-1}L_{EQ}^{-1}}} \\ &+ \frac{\mathrm{T_{LNA}}}{\mathrm{G_{ULN}L_{cable}^{-1}L_{F_1}^{-1}G_{LNA}L_{F_2}^{-1}L_{EQ}^{-1}L_{att}^{-1}}}\end{aligned} \tag{1}$$

$$\mathrm{T_{rx}} = 73\,[\mathrm{K}] \tag{2}$$

The gain of the amplification chain is given by:

$$\mathrm{G_{rx}} = \mathrm{G_{ULN}} + \mathrm{L_{cable}} + \mathrm{L_{filter}} + \mathrm{G_{LNA}} + \mathrm{L_{filter}} + \mathrm{L_{EQ}} + \mathrm{L_{att}} + \mathrm{G_{LNA}} \tag{3}$$

$$\mathrm{G_{rx}} = 65.50\,[\mathrm{dB}] \tag{4}$$

And the system temperature is given by,

$$\mathrm{T_{sys}} = \mathrm{T_{rx}} + \mathrm{T_A} = 161\,[\mathrm{K}] \tag{5}$$

3.3 Digital backend

Figure 8 illustrates the signal-processing architecture of the ARTE digital backend, excluding the radio receiver stage. The system begins with four Analog-to-Digital Converters (ADCs), which digitize the signals received from the main antenna array using 8-bit real sampling. The digitized data are subsequently channelized via an FFT-based spectrometer. Two of the three subarrays are coherently combined in the beamforming stage to synthesize the primary beam, producing the characteristic elliptical beam pattern. The third subarray is used for source localization through the DoA algorithm.

To mitigate the impact of RFI, an omnidirectional reference antenna continuously monitors the local radio environment. The beamformed signal and the reference antenna data are processed by autocorrelation and cross-correlation modules, and the resulting correlation products are analyzed by the RFI ranking algorithm.[17] This procedure enables interference-contaminated channels to be identified and flagged, allowing the system to distinguish between signals of astronomical origin and RFI before candidate generation.

Following the beamforming, the spectra are integrated over 10 ms intervals. The accumulated spectra are stored and transferred to disk through a 10 GbE optical fiber for offline analysis.

In parallel, the beamformed signal undergoes power detection and channel reduction, decreasing the spectral resolution from 2048 to 64 frequency channels. The reduced data are then processed by eleven independent real-time dedispersion pipelines. Each pipeline applies frequency-dependent delays (computed using Equation 6, which depends on the DM and the dispersion constant[18] $\mathcal{D} \simeq 4.1488 \times 10^6\,\mathrm{ms\,MHz^2\,cm^3\,pc^{-1}}$) corresponding to a specific DM trial, generating a dedispersed power time series. Moving-average and variance estimators are subsequently used to compute adaptive detection thresholds. Candidate events are identified when the dedispersed power exceeds the corresponding threshold. The resulting trigger information is combined with the outputs of the RFI ranking and DoA modules to generate candidates for potential FRB-like events.

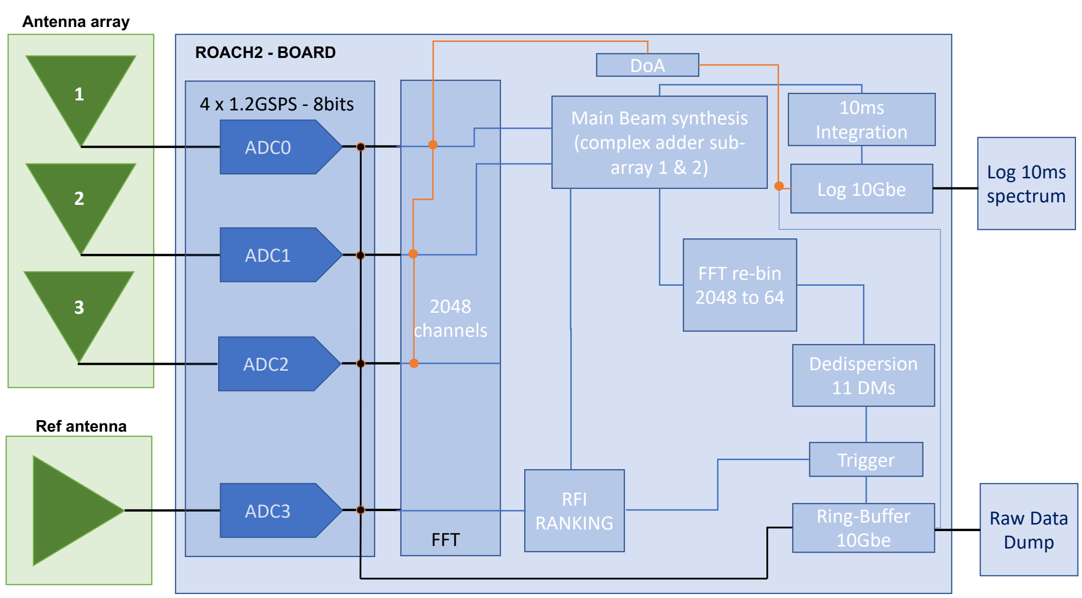

Figure 8: Block diagram of the ARTE backend. Signals from the three subarrays are digitized and channelized via FFT before entering the real-time processing pipeline. Subarrays 1 and 2 are used to synthesize the primary beam, which is integrated, stored, and processed by eleven real-time dedispersion pipelines for transient detection. Detection triggers the dump of the temporal data, which is continuously saved in a ring buffer for offline analysis. Subarray 3 is incorporated for DoA estimation. An independent reference antenna provides statistical discrimination between celestial signals and RFI.

$$\Delta \mathrm{t} \simeq 4.1488 \cdot 10^6 \cdot \left(\mathrm{f_{ref}^{-2}} - \mathrm{f_{chan}^{-2}}\right) \cdot \mathrm{DM} \tag{6}$$

4. ASSEMBLY AND INTEGRATION

After the individual design and verification of each subsystem, the ARTE instrument was assembled and integrated in the Meridiano building at the National Astronomical Observatory, as is shown in Figure 9. This process involved the installation of the antenna array and the equatorial mount from three meters above the floor, the radio receiver, the deployment of the digital backend, and the verification of end-to-end communication between all subsystems. During the first months, the instrument operated pointing at the zenith.

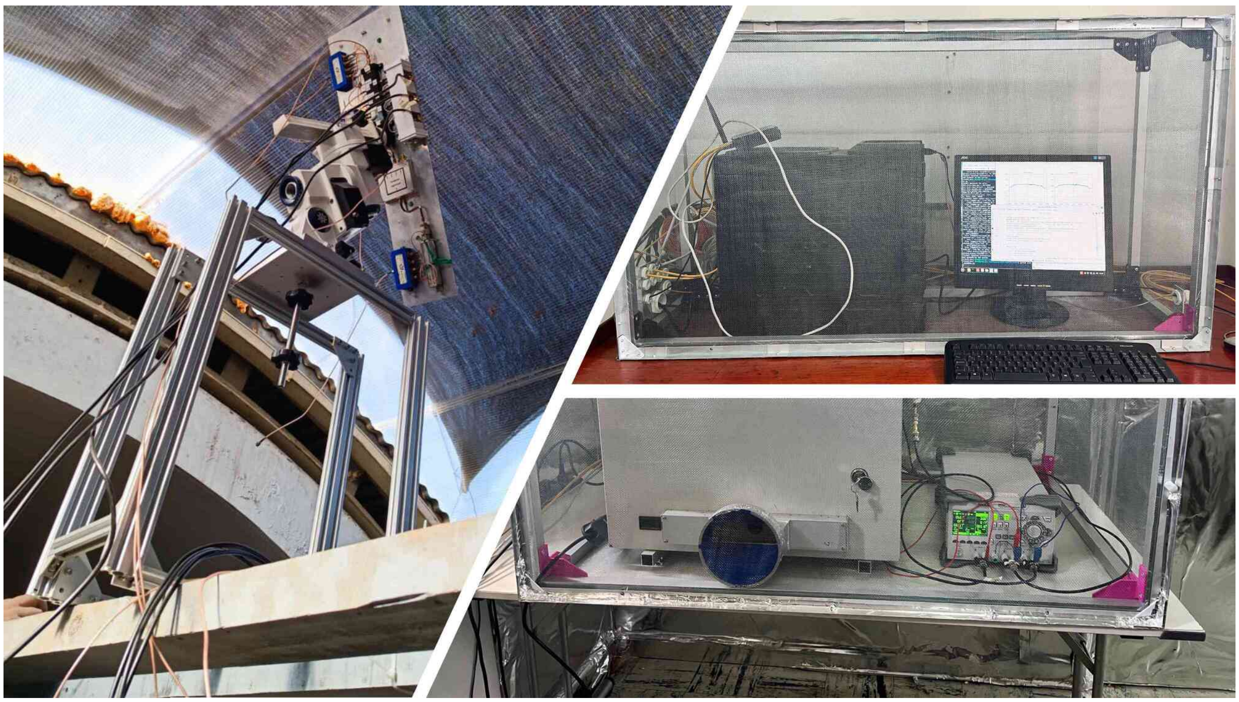

Figure 9: Final assembly of the ARTE radio telescope located at the National Astronomical Observatory of the University of Chile. From left to right, the main antenna array over the equatorial mount and a custom structure to avoid truncating the beam projection on the building. In particular, the aluminum ground plane of the antenna is visible. On the right side, the control room is shown. On the upper side, the operator computer is isolated with a Faraday cage, and on the lower side, the rack, which houses the ROACH2 and the four radio receivers and the power supply for all the electronics, is isolated in a Faraday cage too.

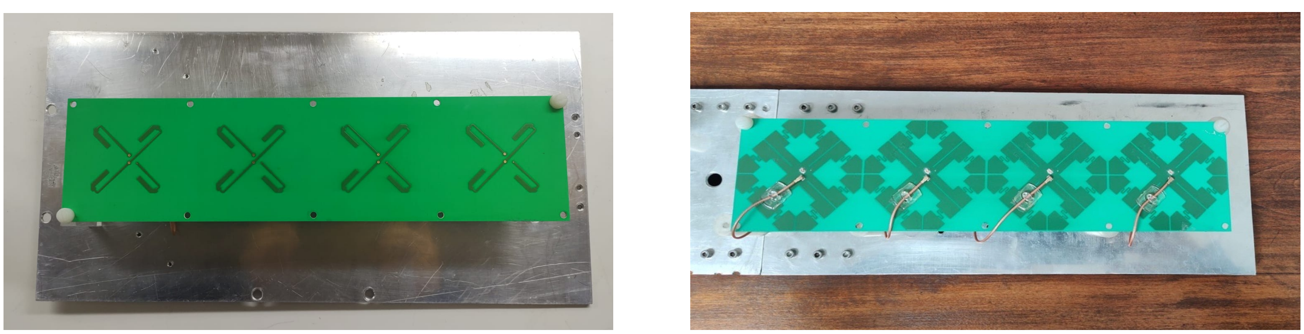

(a) Top view of one sub-array (b) Bottom view of one sub-array.

Figure 10: Subarray of dual polarization dipoles

Figure 10 shows two views of one of the sub-arrays which form the main antenna array: the top and bottom sides. In this view, the IPEX connector corresponding to each polarization of every individual antenna element can be identified in the center of every single element. The antennas were printed in the R04003C substrate.

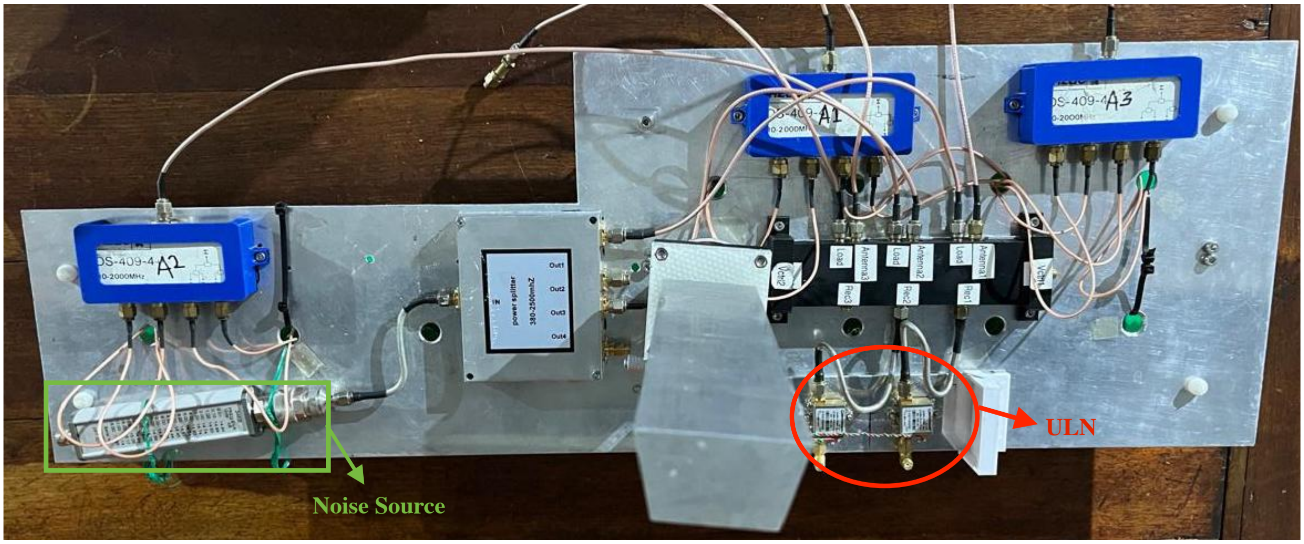

Figure 11: Back plane of the main antenna with the electronics

Figure 11 shows the aluminum ground plane positioned approximately 5 cm behind the antenna array. The holes in the aluminum plane allow the IPEX-to-SMA cables to pass through and connect to the 4:1 analog combiners (blue plastic boxes), one for each sub-array. It should be noted that only one polarization was used during the AIV process.
The Agilent-346B noise source in a green rectangle, shown on the left side of Figure 11, is connected to a 1:4 power splitter. Three of the four outputs are connected to a black enclosure containing three RF switches. Each switch, as shown in Figure 12, has two input ports: one connected to a matched load and the other to the noise source. This configuration enables the hot-cold calibration procedure. The output of each RF switch is then connected to the first ultra-low-noise amplifier (ULN), which constitutes the first amplification stage of the RF signal chain. These amplifiers can also be observed in a red circle in Figure 11. Although only two amplifiers are visible in the photograph, a total of three ULN amplifiers were installed in the system.

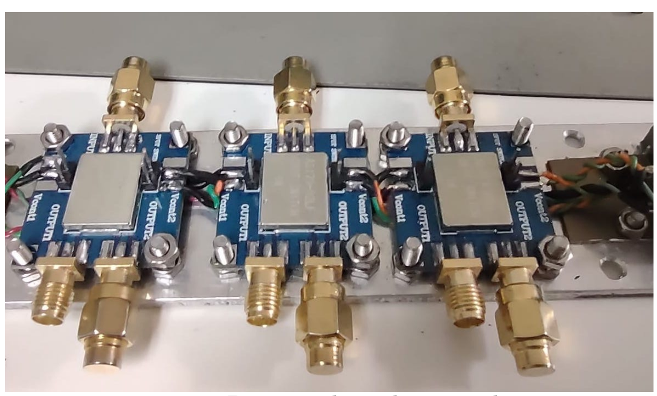

Figure 12: RF switch without enclosure

From the ground plane of the main array, the ULN amplifier shown in Figure 13a is connected to a twelve-meter low-loss SMA cable, which is connected to the radio receiver, which was located in the control room, fully RF isolated. As shows Figure 13 The radio chains are in aluminum independent enclosures and are installed

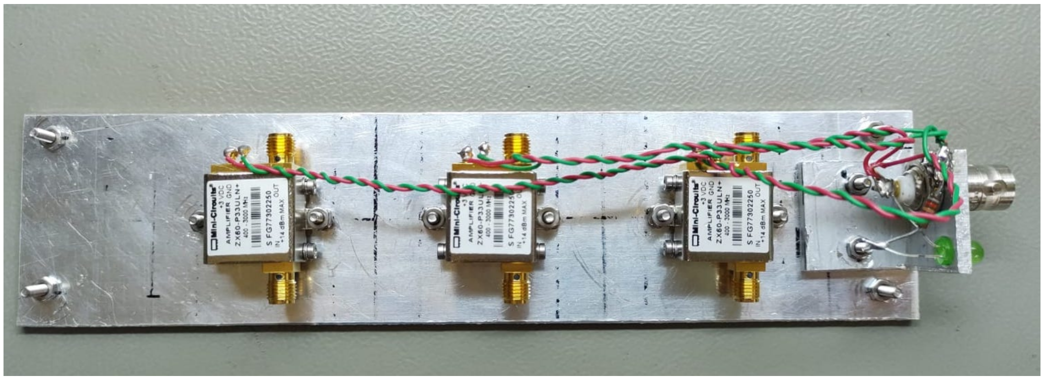

(a) Assembly of ZX60-P333ULN.[12]

(b) Two identical amplification chains in separate enclosures.

Figure 13: Top: ULN amplifier assembly; Bottom:RF amplification system.

inside a rack, as shown on the right side of Figure 9 with the ROACH2. Next to the rack is the power supply, which energizes the whole system. All this electronics is inside a Faraday cage.

Technical challenges during the assembly and integration stage

During the integration phase, several technical challenges were encountered. The main issues and the corresponding mitigation strategies are summarized below:

- **Crosstalk between receiver chains:** Initially, all RF chains were housed within a single enclosure. Due to the high overall gain of the receiver, significant crosstalk was observed between adjacent chains. To mitigate this issue, each RF chain was subsequently installed in an individual aluminum enclosure, providing improved electromagnetic isolation.
- **Intermodulation interference:** The original receiver design included a 3 dB attenuator between the last low-noise amplifier and the ADC. This attenuator was intended to reduce standing waves caused by impedance mismatches and to prevent saturation. During testing, however, intermodulation products were observed, indicating that the final amplification stage was occasionally operating in the nonlinear region. Since the final amplifier exhibits a relatively low IP_{3dB}, the attenuation scheme was redesigned. The 3 dB attenuator was replaced with a 20 dB attenuator located between the equalizer and the final amplifier, effectively reducing the input power level and preventing amplifier saturation.
- **Relocation of the first amplifier stage:** During system integration, the receiver and antenna were relocated to reduce the impact of the RFI. This modification increased the separation between both subsystems to more than 8 m, requiring approximately 12 m of RF cabling. Because the overall noise performance of a cascade receiver is dominated by the first amplification stage, the ZX60-P333ULN ULN amplifier was moved to the antenna ground plane and configured as the first element in the RF chain. This arrangement minimized the contribution of the cable losses to the system noise temperature. Consequently, the final receiver design incorporated a 12 m low-loss coaxial cable between the antenna and the remaining receiver electronics.

5. VERIFICATION AND COMMISSIONING

5.1 Verification with controlled signals

Synthetic pulses injected in ARTE data and recovered using PRESTO[19]

As described in Subsection 3.3, the digital backend archives spectral data with a time resolution of 10 ms. Figure 14 presents synthetic pulses injected into the data using a software routine, allowing the generation of signals with a predefined dispersion measure by controlling the delay. The first example, shown in Figure 14a, was generated with a DM of 270 pc cm^{-3}, while the second case uses a DM of 260 pc cm^{-3}. The resulting datasets were processed using PRESTO, and based on these results, the corresponding dynamic spectra were produced. The primary objective of this initial validation stage was to evaluate the feasibility of using PRESTO

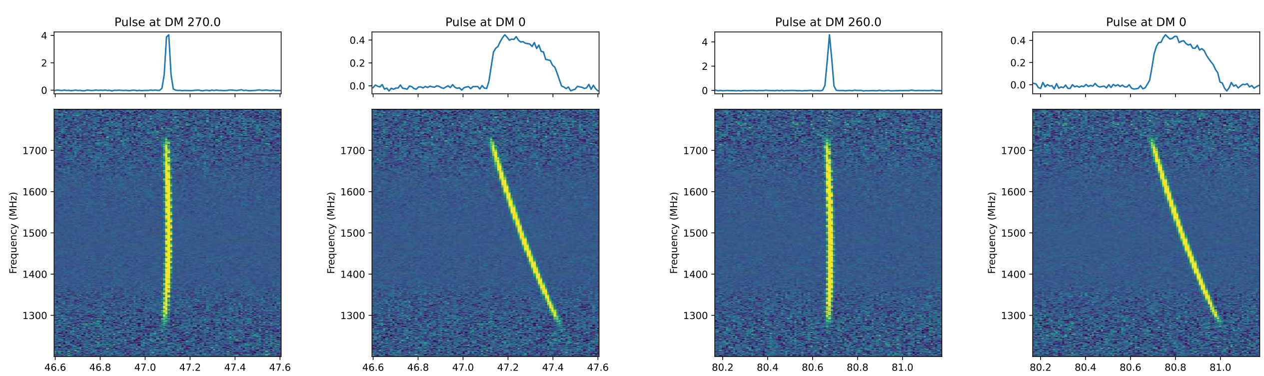

(a) Candidate at 47.1 s with σ 34.28 (b) Candidate at 80.67 s with σ 33.76

Figure 14: Dynamic spectra of synthetic pulses injected in ARTE data

to analyze ARTE archival data and to confirm that synthetic dispersed pulses injected into the data could be correctly identified by the pipeline.

Transmitted pulses (external antenna) and successfully recovered

Figure 15 presents the dynamic spectra of two transmitted pulses detected in the ARTE data. The first example, shown in Figure 15a, corresponds to a pulse with a DM of 200 pc cm^{-3}, while the second example, shown in Figure 15b, has a DM of 190 pc cm^{-3}. To generate these signals, a Zynq UltraScale + RFSoC[20] (Radio Frequency System-on-Chip) device was used to produce FRB-like pulses in the analog domain, which were transmitted through a highly directive antenna toward the ARTE radio telescope. The recorded datasets were subsequently analyzed with PRESTO, following the successful validation of the software-based injection tests. The primary objective of this stage was to verify the correct functioning of the complete acquisition and processing pipeline, from the reception of the transmitted signal by the telescope to its archival and subsequent detection in the recorded data.

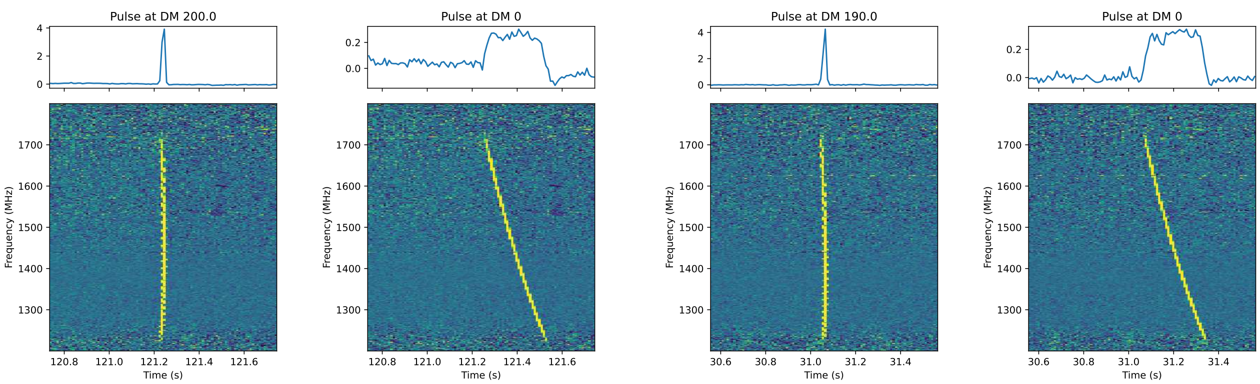

(a) Candidate at 121.24 s with σ 81.36

(b) Candidate at 31.06 s with σ 77.23

Figure 15: Dynamic spectra of analog-transmitted pulses detected in the ARTE data

The color scale is intentionally omitted from the dynamic spectra shown in Figures 14 and 15, as the objective of this analysis is to demonstrate the successful detection and identification of the injected and transmitted pulses rather than to quantify their intensity or flux calibration.

5.2 RFI characterization

Following the validation of the detection pipeline, preliminary RFI characterization studies were conducted using ARTE on-sky observations. These initial analyses focus on representative sources of man-made signals.

Dynamic spectra of a weather satellite and SAOCOM radar transit

Figure 16 presents two dynamic spectra corresponding to different identified RFI events. Figure 16a shows the transit of a meteorological satellite, whose emissions are detected between approximately 1.68 and 1.74 GHz. Figure 16b shows the transit of SAOCOM (Satélite Argentino de Observación Con Microondas), whose transmission is observed at approximately 1.275 GHz as the satellite passes through the field of view of the ARTE radio telescope.

The vertical axis shows the observing frequency in MHz, while the horizontal axis represents time in minutes. For both figures, the upper panel presents the antenna temperature averaged over all unflagged spectral channels. In the dynamic spectrum, the color scale represented the normalized antenna temperature, $\frac{T_A - \tilde{T}_A}{\sigma_T}$, where $\tilde{T}_A$ and σ_T denote the temporal median and temporal standard deviation, respectively, computed independently for each frequency channel. Moreover, the green horizontal lines spanning specific frequency channels indicate frequency ranges that have been flagged due to persistent RFI and masked in the visualization to prevent saturation of the dynamic spectrum, thereby improving visibility of weaker signals. Each plot covers a five-minute interval.

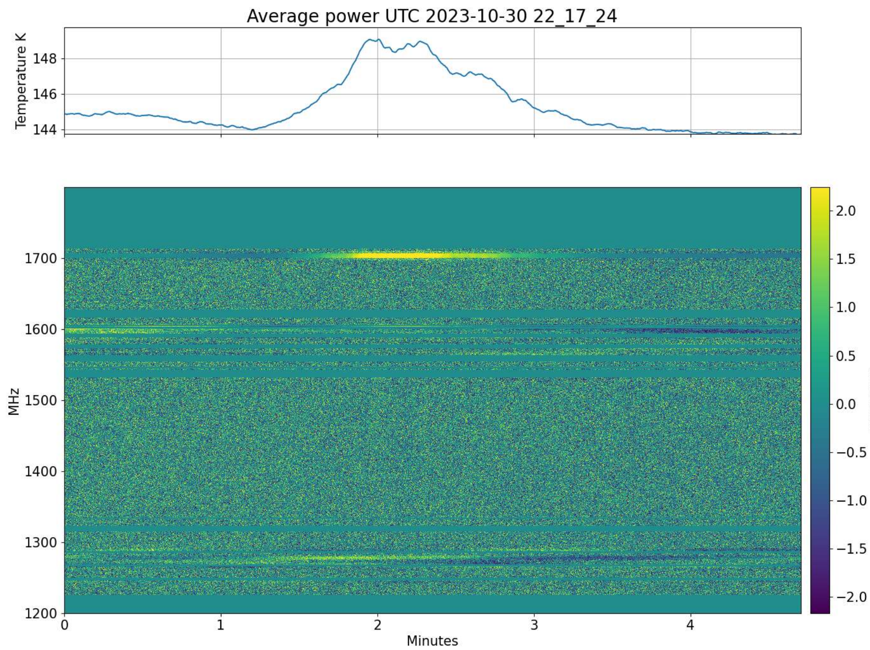

(a) Weather satellite transit.

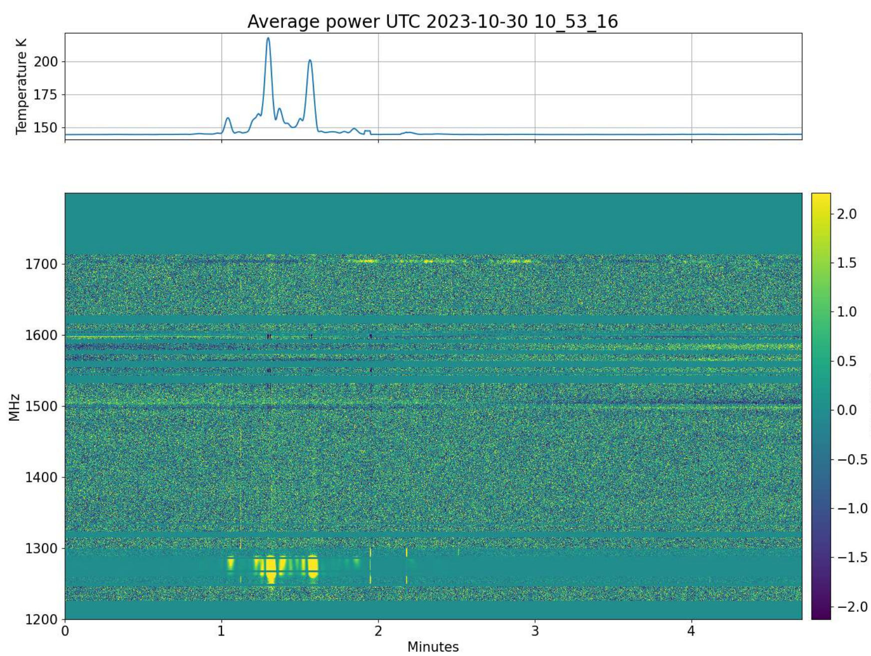

(b) SAOCOM transit.

Figure 16: Dynamic spectra of a weather satellite and SAOCOM radar transits. For each panel, the upper subplot shows the antenna temperature averaged over all unflagged spectral channels, while the lower subplot displays the normalized dynamic spectrum.

5.3 Qualitative validation using a solar flare event

Figure 17 shows the comparison between the dynamic spectrogram of ARTE (upper panel) and the EOVSA[21,22] (lower panel). ARTE dynamic spectra exhibit black horizontal lines at specific frequencies, corresponding to channels that were flagged due to the identified presence of RFI. The color scale represents the normalized antenna temperature after subtraction of the temporal median and normalization by the temporal standard deviation of each frequency channel. The frequency axis spans from 1200 to 1800 MHz. The horizontal axis shows time in minutes, reflecting the long duration of the observed event.

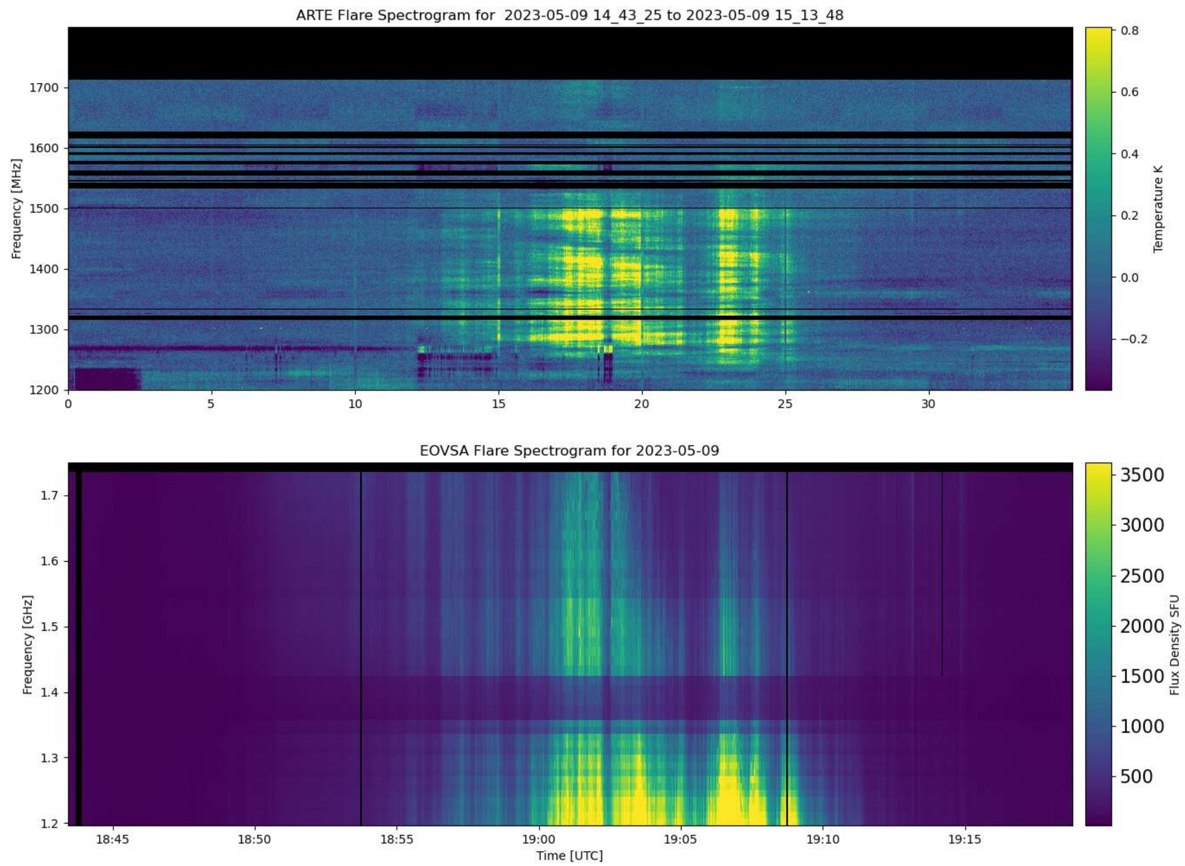

Figure 17: Dynamic spectrograms of the first astronomical detection obtained with ARTE during its commissioning phase in May 2023 (upper panel) and the corresponding EOVSA observation (lower panel). The event is a long-duration GOES M4.2-class solar flare observed across the full L-band. The flare reached a peak flux density above 10^4 kJy at around 1212.7 MHz and lasted approximately 35 minutes. The agreement between the temporal and spectral structures observed by both instruments confirms the successful astronomical detection and validates the ARTE calibration and data-processing pipeline.

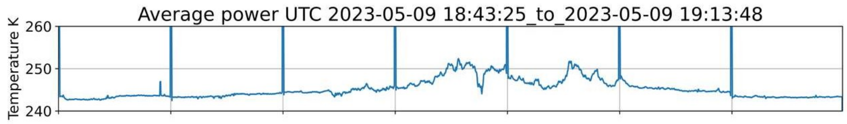

(a) Antenna average power detected by ARTE.

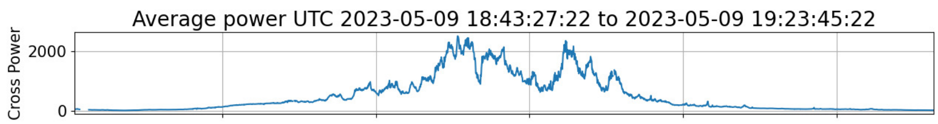

(b) Cross power reported by EOVSA.

Figure 18: Comparison between the ARTE average antenna temperature and EOVSA cross-power measurements during the first solar flare detected by ARTE, whose dynamic spectrum is presented in Figure 17. The measurements span approximately 35 minutes, covering the full duration of the event. The ARTE curve corresponds to the antenna temperature averaged over all valid spectral channels, while the EOVSA curve represents the corresponding cross-power measurement. Although the two instruments measure different quantities, both datasets exhibit a similar temporal evolution throughout the flare. Vertical features appearing at 5-minute intervals in the ARTE data are artifacts introduced by the periodic hot-ambient calibration procedure.

The detection was independently verified using the EOVSA flare catalog and associated observations available through the EOVSA public archive http://www.ovsa.njit.edu/wiki/index.php/File:EOVSA_20230509_M4flare_log.png. The comparison is intended to provide a qualitative assessment of the observed spectral and temporal features, rather than a direct quantitative comparison, as the two instruments differ significantly in sensitivity, frequency coverage, and calibration procedures.

6. CONCLUSIONS

ARTE was successfully assembled, integrated, and commissioned as a compact radio telescope for the detection of Galactic Fast Radio Bursts like events. Throughout the commissioning phase, several modifications to the radio receiver chain were implemented to optimize system performance. These included relocating the ultra-low-noise amplifier to the antenna ground plane to compensate for cable losses, introducing additional attenuation to prevent amplifier saturation caused by intermodulation effects, and isolating each receiver chain within individual aluminum enclosures to mitigate crosstalk.

The final system achieved amplitude imbalances below ± 0.5 dB, phase imbalances below $\pm 5°$, and a system noise temperature of approximately 161 K. A complete post-processing pipeline was developed to perform calibration, baseline removal, and the generation of absolute-power dynamic spectra from data acquired every 10 ms. The detection capabilities of the instrument were validated through the injection of synthetic FRB signals both at the antenna input and into recorded data streams, demonstrating reliable event recovery under realistic observing conditions.

RFI was identified as one of the principal challenges during deployment. To mitigate its impact, additional electromagnetic shielding measures were implemented, including the installation of a Faraday cage and the relocation of the receiver electronics to a shielded room. Several sources of interference within the operational band were identified and characterized, including cellular communications, GPS transmissions, weather satellites, and synthetic aperture radar systems. The successful detection of a solar flare provided the first astronomical validation of the instrument and confirmed the expected sensitivity of the system.

Further work will focus on improving the sensitivity and automation of ARTE through the integration of the already developed DoA algorithm and the implementation of a second polarization receiver chain and corresponding digital backend path to enable full dual-polarization observations.

APPENDIX A. SYSTEM PERFORMANCE METRICS

In this section, all calculations are carried out at 1.5 GHz; therefore, all frequency-dependent quantities are consistently evaluated at this frequency. The analysis assumes a single polarization.

Sensitivity calculations

$$\Gamma = \frac{\mathrm{A_e}}{2\mathrm{k_B}} \tag{7}$$

From Figure 5, the Gain is 14.4 dBi; however, a 1 $mathrmdB$ loss should be considered due to the cables and combiners. Therefore, replacing in the Equation 7 it is obtained that:

$$\Gamma = 2.5 \cdot 10^{-5} [\,\mathrm{K\,Jy^{-1}}\,] \tag{8}$$

Fluence calculations

$$\mathrm{F} = \Gamma^{-1} \frac{\mathrm{SNR} \cdot \mathrm{T_{sys}} \cdot \tau}{\sqrt{\Delta\upsilon \cdot \tau}} \tag{9}$$

Where $\Delta\upsilon$ is the bandwidth of interest that in our case is 600 MHz, τ the time resolution of 10 ms, SNR the signal noise ratio, and $\mathrm{t_{sys}}$ the noise temperature of the system, which is 161 K, given by the Equation 5. Finally, using the ARTE parameters:

$$\mathrm{F} = 131.45\,[\mathrm{kJy} \cdot \mathrm{ms}] \tag{10}$$

Effective signal-to-noise ratio

From quantization theory as described by Lyons,[23] the ideal ADC signal-to-noise ratio (SNR) is given by:

$$\mathrm{SNR_{ADC}} = 6.02 \cdot \mathrm{N} + 1.76 \tag{11}$$

As ARTE uses an 8-bit ADC:

$$\mathrm{SNR_{ADC}} = 6.02 \cdot 8 + 1.76 \approx 49.92[\mathrm{dB}] \tag{12}$$

The FFT processing gain (coherent case) is given by:

$$\mathrm{G_{FFT}} = 10 \log_{10} \left(\frac{\mathrm{N_{FFT}}}{2} \right) \tag{13}$$

Where $\mathrm{N_{FFT}}$ is the number of FFT points:

$$\mathrm{G_{FFT}} = 10 \log_{10} \left(\frac{2048}{2} \right) \approx 30.1[\mathrm{dB}] \tag{14}$$

Therefore, the effective SNR per spectral bin:

$$\mathrm{E_{SNR}} = 49.92 + 30.1 = 80.02[\mathrm{dB}] \tag{15}$$

Calibration calculations

The receiver noise temperature was estimated using the Y-factor method,[16] with a calibrated noise source.[24] The effective hot temperature was obtained from the Excess Noise Ratio (ENR) definition:

$$\mathrm{ENR} = 10 \log_{10} \left(\frac{\mathrm{T_{hot}} - \mathrm{T_{amb}}}{\mathrm{T_{amb}}} \right) \tag{16}$$

where, $\mathrm{T_{amb}} = 290\mathrm{K}$. Considering an insertion loss (L) in dB between the noise source and the receiver, the equivalent hot temperature is given by:

$$\mathrm{T_{hot}} = \mathrm{T_{amb}} \left(1 + 10^{\frac{\mathrm{ENR}-\mathrm{L}}{10}} \right) \tag{17}$$

Then the Y-factor is defined as:

$$Y = \frac{P_{hot}}{P_{amb}} \tag{18}$$

The receiver noise temperature is then obtained as:

$$T_{rx} = \frac{T_{hot} - YT_{amb}}{Y - 1} \tag{19}$$

Then, to obtain the receiver noise temperature after the hot-load calibration:

$$T_{rx} = \frac{T_{hot} \cdot P_{amb} - T_{amb} \cdot P_{hot}}{P_{hot} - P_{amb}} \tag{20}$$

ACKNOWLEDGMENTS

This work was supported by the Chilean National Agency for Research and Development (ANID) through its grants Basal ACE210002, FB210003, the National Fund for Scientific and Technological Development FONDECYT 1221662, and CASSACA-CCJRF1901.

EOVSA was designed, built, and is now operated by the New Jersey Institute of Technology (NJIT) as a community facility. EOVSA solar operations are supported by NSF grant AGS-2436999 to NJIT. We acknowledge the use of EOVSA data products for comparison with the observations presented in this work.

Generative AI tools were used to assist with language editing and text refinement. The authors reviewed and validated all technical content and are solely responsible for the final manuscript.

REFERENCES

[1] Solís Garrido, F. A., "Assembly, integration and verification of an astronomy experiment for galactic fast radio burst detection," (2024).

[2] Gallardo, D., Finger, R., Solis, F., Monasterio, D., Jorquera, S., Pizarro, J., Riquelme, J., Curotto, F., Pizarro, F., and Bronfman, L., "An ultra-wideband dual polarization antenna array for the detection and localization of bright fast radio transients in the milky way," (2025).

[3] Bochenek, C. D., McKenna, D. L., Belov, K. V., Kocz, J., Kulkarni, S. R., Lamb, J., Ravi, V., and Woody, D., "Stare2: Detecting fast radio bursts in the milky way," *Publications of the Astronomical Society of the Pacific* **132**, 034202 (Jan. 2020).

[4] Liu, W., Meng, Q., Wang, C., Zhou, C., Yao, S., and Tariq, I., "A real-time, pipelined incoherent dedispersion method and implementation in fpga," *Publications of the Astronomical Society of the Pacific* **134**, 015008 (Jan. 2022).

[5] Xilinx, Inc., *Virtex-6 FPGA LX760, LX550T, LX365T, LX240T, LX195T, LX130T, SX475T, and SX315T CES Errata*. Xilinx, Inc. (2011). Accessed: 2026-06-17.

[6] Petroff, E., Hessels, J. W. T., and Lorimer, D. R., "Fast radio bursts," *The Astronomy and Astrophysics Review* **27** (May 2019).

[7] Lorimer, D. R. and Kramer, M., [*Handbook of Pulsar Astronomy*], vol. 4 of *Cambridge Observing Handbooks for Research Astronomers*, Cambridge University Press, Cambridge (2005).

[8] Bochenek, C. D., Ravi, V., Belov, K. V., Hallinan, G., Kocz, J., Kulkarni, S. R., and McKenna, D. L., "A fast radio burst associated with a galactic magnetar," *Nature* **587**, 59–62 (Nov. 2020).

[9] CASPER Collaboration, "Roach-2 revision 2." https://casper.berkeley.edu/wiki/ROACH-2_Revision_2 (2026). Accessed: 2026-06-12.

[10] Petroff, E., Hessels, J. W. T., and Lorimer, D. R., "Fast radio bursts at the dawn of the 2020s," *The Astronomy and Astrophysics Review* **30** (Mar. 2022).

[11] Prieto Carvajal, M., "Diseño, implementación y caracterizacion de un receptor astronomico de microondas para la deteccion de rafagas rapidas de radio (frb) en la via lactea," (2021).

[12] Mini-Circuits, "Zx60-p33uln+ low noise amplifier datasheet." https://www.minicircuits.com/pdfs/ZX60-P33ULN+.pdf (2026). Accessed: 2026-06-02.

[13] Mini-Circuits, "Zx60-2534ma+ low noise amplifier datasheet," (2026). https://www.minicircuits.com/pdfs/ZX60-2534MA+.pdf (accessed 2026-06-02).
[14] Mini-Circuits, "Zeq-8-222s+ equalizer datasheet." https://www.minicircuits.com/pdfs/ZEQ-8-222S+.pdf (2026). Accessed: 2026-06-02.
[15] Mini-Circuits, "Vat-20+ fixed attenuator datasheet." https://www.minicircuits.com/pdfs/VAT-20+.pdf (2026). Accessed: 2026-06-02.
[16] Pozar, D. M., [*Microwave engineering*], John wiley & sons (2012).
[17] Bravo, D., *Design, Implementation and Testing of a real-time electromagnetic interference detector and classifier for the five-hundred-meter aperture spherical telescope (FATS)*, Master's thesis, Universidad de Chile (2021).
[18] Lyne, A. and Graham-Smith, F., [*3 Telescopes and techniques*], Cambridge Astrophysics, Cambridge University Press (2012).
[19] Ransom, S. M. and Contributors, P., "Presto: Pulsar exploration and search toolkit." https://github.com/scottransom/presto (2026). Accessed: 2026-06-16.
[20] Advanced Micro Devices, Inc., *Zynq UltraScale+ RFSoC Data Sheet: Overview*. AMD (2024). Accessed: 2026-06-17.
[21] Gary, D. E., Chen, B., Dennis, B. R., Fleishman, G. D., Hurford, G. J., Krucker, S., McTiernan, J., Nita, G. M., White, S. M., and Yu, S., "Microwave and hard x-ray observations of the 2017 september 10 solar limb flare," *The Astrophysical Journal* **863**(1), 83 (2018).
[22] Gary, D. E., Nita, G. M., White, S. M., Hurford, G. J., McBride, W., Fleishman, G. D., Chen, B., Brosius, J. W., and Krucker, S., "The expanded owens valley solar array (eovsa): Overview and first results," *Solar Physics* **293**, 129 (2018).
[23] Lyons, R. G., [*Understanding Digital Signal Processing*], Prentice Hall, Upper Saddle River, NJ, USA, 3 ed. (2011).
[24] Keysight Technologies, "346b noise source datasheet." https://www.testequipmenthq.com/datasheets/Keysight-346B-Datasheet.pdf (2026). Accessed: 2026-06-16.